Local Modulation of Electrical Distributions in Bent PS Fibers via Multi-segmented Layered Structures

Zelin Xu[1], Kai Fang[1], Tiqing Wang[1], Peng Li[1], Dianzi Liu[2], Iren E. Kuznetsova[3], Tingfeng Ma[4] and Zhenghua Qian[1†]

[1*]State Key Laboratory of Mechanics and Control of Aerospace Structures, College of Aerospace Engineering, Nanjing University of Aeronautics and Astronautics, Nanjing, 210016, China.
[2]School of Engineering, University of East Anglia, Norwich, NR4 7TJ, U.K..
[3]Kotel'nikov Institute of Radio Engineering and Electronics of RAS, Moscow, 125009, Russia.
[4]Key Laboratory of Impact and Safety Engineering, Ministry of Education, Ningbo University, Ningbo, 315211, China.

[†]Corresponding author, Email: qianzh@nuaa.edu.cn

Abstract

Piezoelectric semiconductor (PS) fibers are the foundation of nanogenerators, nano force sensors, and other nanodevices. Regulating the local piezopotential characteristics inside the PS fiber is crucial for its piezoelectric performance. However, due to the extremely small size of nanofibers, this is quite challenging. In this study, we propose a method for modulating local electrical distribution of bent PS fibers using a multi-segmented layered structure. The field equations for bent PS fibers are derived, and the effect of a non-uniform additional layer's discontinuity in material properties and thickness distributions on the distributions of strain, potential, and charge carrier concentration fields within the fiber are investigated. Results from theoretical studies and case studies indicate that the discontinuity of material coefficients or the thickness in the attached layer allows the local piezopotential distribution of the bent fiber to be effectively tuned by external forces. In the bent fibers,

the potential and carrier concentration in the intermediate region no longer remain constant, but instead, localized potential wells and barriers, or plateau-like regions of high and low potential, start to form along the axial direction, and they are symmetric with respect to the strain neutral axis. The discontinuity of various material coefficients in the attached layer has different effects on the local potential changes in the bent fiber. Local potentials of arbitrary form can be controlled through different material and thicknesses distribution combinations of the attached layer. The findings of this study provide important guidance for modulating the local electrical distributions of PS fibers and offer new insights and design ideas for nanoscale piezoelectric devices.

Keywords: electrical modulation, potential adjustment, bending deformation, piezoelectric semiconductor (PS)

1 Introduction

Piezoelectric semiconductor (PS) materials exhibit both piezoelectric and semiconductor properties, allowing for the control of their electrical behavior through mechanical loading. Many PS structures have been synthesized [1–3] and used in various devices, such as nanogenerators [4, 5], piezoelectric effect transistors [6, 7], physical and chemical sensors [8, 9], and piezoelectric logic nanodevices [10]. The theoretical development of PS structures has been rapid, with rich results in both fundamental theory and applied science. The comprehensive research on PS-related theory provides a reliable foundation for the development of piezoelectric crystal devices.

Compared with other structures such as thin films and tubes, one-dimensional fibers are the most interesting structure for researchers [11, 12]. PS fibers are easier to manufacture and can withstand greater mechanical deformation [13], making their electromechanical behavior, including vibration [14, 15], bending [16], stretching [17, 18], and torsion [19], widely studied, with valuable results for device design.

The bent nanofibers are widely used in piezoelectric devices such as nanogenerators and sensors. The renowned ultrasonic-sound nanogenerator invented by Wang [20] is based on bent deformed PS one-dimensional fibers. The schematic diagram of the structural principle of the nanogenerator is shown in Figure 1. As shown in Figure 1(a), its basic structure is to cover a layer of silicon electrode coated with platinum metal on an array composed of ZnO nanofibers. The platinum coating not only enhances the electrode conductivity, but also forms a Schottky contact with the semiconductor. Some ZnO nanofibers are in contact with the upper electrode, while others are located between the electrode teeth. Under the action of ultrasound, the electrode moves downward, causing the fibers to bend transversely, resulting in a partial forward bias of the Schottky junction and thus generating a current. The bending of a single fiber is shown in Figure 1(b).

Composite structures are commonly employed in piezotronics [21–23]. Studies have shown that the use of insulating layers can improve the efficiency of nanogenerators [24–26]. Wrapping the nanofibers with an insulating polymer layer can not only prevent internal discharge caused by contact between the nanofibers but also improve the stability and durability of the device, at the same time, effectively enhancing the output voltage [27]. Theoretical analyses have been conducted to investigate the electromechanical coupling fields [18, 28] and wave propagation characteristics [29–31] in PS composite structures, providing more options for materials and structures in piezotronic device fabrication.

Inspired by these works, we aim to modulate the local piezoelectric distribution in the fiber by utilizing the discontinuity of the material coefficient and thickness of the attached insulation elastic layer, based on the actual design of the piezoelectric semiconductor fiber wrapped in an insulation shell. In this paper, local piezoelectric polarization discontinuity is artificially constructed in the multi-segmented layered fiber structure, thereby changing the local piezoelectric potential inside the fiber and achieving control over the fiber's piezoelectric performance.

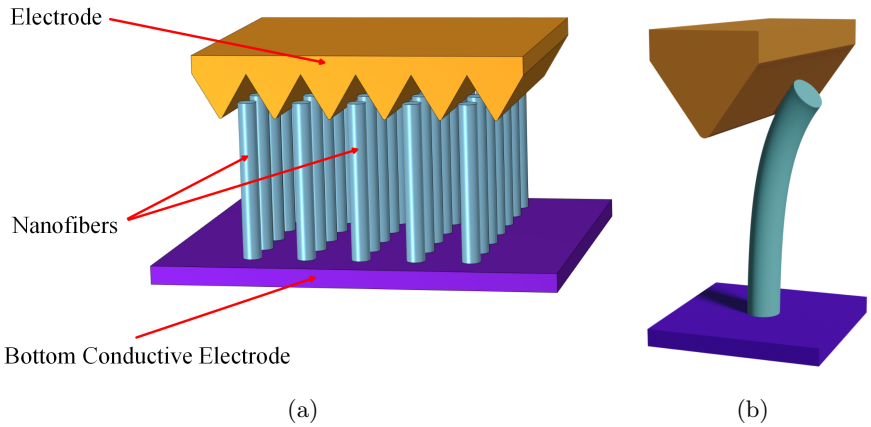

Figure 1: Nanogenerator model: (a) Schematic illustration of the zigzag electrode and nanofibers; (b) Single fiber bent by electrode propulsion;

This paper presents a feasible design scheme using a three-layer PS fiber, with the middle layer being the PS layer and the upper and lower elastic layers having non-uniform elastic constants. The left end face of the fiber is fixed, and the right end face is subjected to shear force. The novelty of this paper lies in the fact that significant control over the potential distribution of the intermediate PS layer can be achieved solely by manipulating the elastic properties and thickness of the additional layer. By combining various control strategies, it becomes possible to achieve a diverse range of desired control objectives. In

Section 2, we will model and derive the one-dimensional coupling equations of the proposed composite fiber and perform corresponding theoretical solutions. In Section 3, we conduct numerical studies on fiber models with different elastic parameters and thicknesses and compare their modulation effects on local potential. Finally, we summarize our findings in Section 4.

2 Multi-segmented layered structure's coupling equation

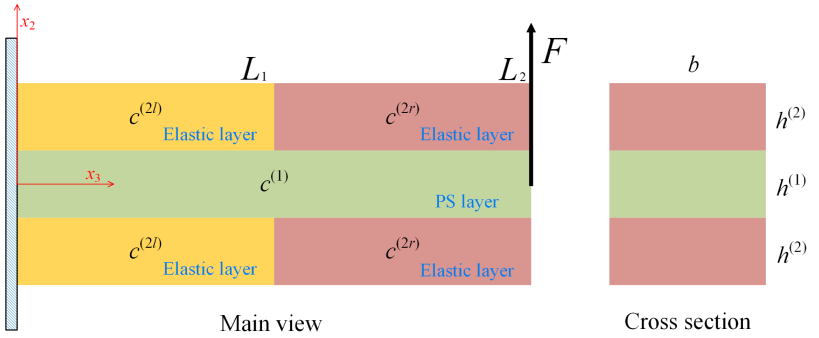

Figure 2: A schematic of the bent multi-segmented layered structure with varying elastic layer elastic coefficients.

The crucial aspect of local piezoelectric modification lies in creating localized discontinuity within the piezoelectric polarization. As is commonly understood, piezoelectric polarization is induced by strain. This approach is based on the principle that, under equivalent stress, the strain produced by regions with lower stiffness is always greater than that of those with higher stiffness, thereby generating discontinuous strain. To ensure that the neutral layer remains on the PS layer during bending deformation, the attached elastic layer is symmetrically distributed above and below the PS layer. The equivalent cantilever beam model of the multi-segmented layered PS structure is shown in Figure 2. This paper proposes a multi-segmented layered structure that features non-uniform stiffness distribution. Specifically, two fully covered and segmented elastic layers are attached to the middle PS layer. Adding attached elastic layers above and below the PS layer of the nanofiber is necessary to maintain the neutral plane in the middle during bending and to ensure that the PS fiber is sandwiched in the insulating elastic layer, which is in line with the realistic design of the ultrasonic motor.

The intermediate PS layer in this uniform structure simultaneously exhibits piezoelectric and semiconductor characteristics, whose material parameters are denoted by superscript $^{(1)}$. Its polarization direction c-axis is oriented along the positive direction of the x_3-axis, while its axial elastic constant, piezoelectric

constant, and dielectric constant are designated as c^1, e_{33}^1, and ε_{33}^1, respectively. The height of the middle PS layer is $h^{(1)}$. The elastic layer, attached both above and below, is comprised of two sections with varying stiffness levels. To simplify matters, we assume the layer is purely elastic and electrically insulating, devoid of any piezoelectric or semiconductor properties. The attached elastic layer has a height of $h^{(2)}$ and is divided into two sections of length L_1 and $L_2 - L_1$ on the left and right, respectively. The superscript $^{(2)}$ indicates the material parameters of the elastic layer, while the superscripts $^{(l)}$ and $^{(r)}$ indicate the material parameters of the left partially and partially elastic layer. In such cases, it suffices to only consider the elastic constant $c^{(2)}$ among the major constants, as this is a common practice in the analysis of piezoelectric multi-layer structures [32, 33]. This approach enables sufficient proof that manipulating local electrical behavior can be achieved through the utilization of material heterogeneity. It is important to note that in our simulation, c takes on different values in the two sections, which we have labeled as $c^{(2l)}$ and $c^{(2r)}$.

Considering the deformation in the x_2-x_3 plane of this structure, and referring to the Mindlin plate theorem, power series expansions of the displacement, potential, and carrier concentration variations with first-order approximation are written in the following form:

$$\begin{aligned} u_2 &\cong \nu(x_3,t) \\ u_3 &\cong x_2\psi(x_3,t) \\ \varphi &\cong x_2\phi^1(x_3,t) \\ \Delta n &\cong x_2 n^1(x_3,t) \\ \Delta p &\cong x_2 p^1(x_3,t) \end{aligned} \tag{1}$$

The corresponding strain, electric field, and carrier concentration gradients can be expressed as:

$$\begin{aligned} &S_3 = S_{33} = x_2\psi_{,3} \quad S_4 = 2S_{23} = \nu_{,3} + \psi \\ &E_2 = -\phi^1 \quad E_3 = -x_2\phi^1_{,3} \\ &\Delta n_{,2} = n^1 \quad \Delta n_{,3} = x_2 n^1_{,3} \\ &\Delta p_{,2} = p^1 \quad \Delta p_{,3} = x_2 p^1_{,3} \end{aligned} \tag{2}$$

The stresses and electric displacements in the piezoelectric and elastic layers are expressed as:

$$\begin{aligned} T_3^{(1)} &= c_{33}^{(1)} S_3 - e_{33}^{(1)} E_3 = c_{33}^{(1)} x_2\psi_{,3} + e_{33}^{(1)} x_2\phi^1_{,3} \\ T_4^{(1)} &= c_{44}^{(1)} S_4 - e_{15}^{(1)} E_2 = c_{44}^{(1)}(\nu_{,3} + \psi) + e_{15}^{(1)}\phi^1 \\ D_2^{(1)} &= e_{15}^{(1)} S_4 + \varepsilon_{11}^{(1)} E_2 = e_{15}^{(1)}(\nu_{,3} + \psi) - \varepsilon_{11}^{(1)}\phi^1 \\ D_3^{(1)} &= e_{33}^{(1)} S_3 + \varepsilon_{33}^{(1)} E_3 = e_{33}^{(1)} x_2\psi_{,3} - \varepsilon_{33}^{(1)} x_2\phi^1_{,3} \\ T_3^{(2)} &= c_{33}^{(2)} S_3 = c_{33}^{(2)} x_2\psi_{,3} \\ T_4^{(2)} &= c_{44}^{(2)} S_4 = c_{44}^{(2)}(\nu_{,3} + \psi) \end{aligned} \tag{3}$$

The material constants of the PS layers in Equation (3) also satisfy the following relationship:

$$\begin{array}{ll} c_{33}^{(1)}=1/s_{33}^{E(1)} & c_{44}^{(1)}=1/s_{44}^{E(1)} \\ e_{33}^{(1)}=d_{33}^{(1)}/s_{33}^{E(1)} & e_{15}^{(1)}=d_{15}^{(1)}/s_{44}^{E(1)} \\ \varepsilon_{11}^{(1)}=\varepsilon_{11}^{T(1)}-(d_{15}^{(1)})^2/s_{44}^{E(1)} & \varepsilon_{33}^{(1)}=\varepsilon_{33}^{T(1)}-(d_{33}^{(1)})^2/s_{33}^{E(1)} \end{array} \tag{4}$$

The drift-diffusion equations for the current in the PS layer are:

$$\begin{array}{l} J_2^n=qn_0\mu_{22}^nE_2+qD_{22}^n\Delta n_{,2}=-qn_0\mu_{22}^n\phi^1+qD_{22}^nn^1 \\ J_3^n=qn_0\mu_{33}^nE_3+qD_{33}^n\Delta n_{,3}=-qn_0\mu_{33}^nx_2\phi_{,3}^1+qD_{33}^nx_2n_{,3}^1 \\ J_2^p=qp_0\mu_{22}^nE_2-qD_{22}^p\Delta p_{,2}=-qp_0\mu_{22}^n\phi^1-qD_{22}^np^1 \\ J_3^p=qp_0\mu_{33}^nE_3-qD_{33}^p\Delta p_{,3}=-qp_0\mu_{33}^nx_2\phi_{,3}^1-qD_{33}^nx_2p_{,3}^1 \end{array} \tag{5}$$

Since the cross-section of the multi-segmented layered structure assumed in this paper is rectangular [34], the bending moment M, shear force Q, and the equivalent potential shift sum in the structure can be obtained from the following integral relationship:

$$\begin{array}{ll} M=T_{33}^{[1]} & =b\int_{-h^{(1)}/2-h^{(2)}}^{h^{(1)}/2+h^{(2)}}x_2T_3dx_2 \\ & =b\int_{-h^{(1)}/2-h^{(2)}}^{-h^{(1)}/2}x_2T_3^{(2)}dx_2+b\int_{-h^{(1)}/2}^{h^{(1)}/2}x_2T_3^{(1)}dx_2+b\int_{h^{(1)}/2}^{h^{(1)}/2+h^{(2)}}x_2T_3^{(2)}dx_2 \\ & =\frac{2}{3}[(\frac{h^{(1)}}{2}+h^{(2)})^3-(\frac{h^{(1)}}{2})^3]bc_{33}^{(2)}\psi_{,3}+\frac{2}{3}(\frac{h^{(1)}}{2})^3bc_{33}^{(1)}\psi_{,3}+\frac{2}{3}(\frac{h^{(1)}}{2})^3be_{33}^{(1)}\phi_{,3}^1 \\ Q=T_{32}^{[0]} & =b\int_{-h^{(1)}/2-h^{(2)}}^{h^{(1)}/2+h^{(2)}}T_4dx_2 \\ & =b\int_{-h^{(1)}/2-h^{(2)}}^{-h^{(1)}/2}T_4^{(2)}dx_2+b\int_{-h^{(1)}/2}^{h^{(1)}/2}T_4^{(1)}dx_2+b\int_{h^{(1)}/2}^{h^{(1)}/2+h^{(2)}}T_4^{(2)}dx_2 \\ & =2bh^{(2)}c_{44}^{(2)}(\nu_{,3}+\psi)+bh^{(1)}c_{44}^{(1)}(\nu_{,3}+\psi)+bh^{(1)}e_{15}^{(1)}\phi^1 \\ D_2^0=D_2^{[0]} & =b\int_{-h^{(1)}/2}^{h^{(1)}/2}D_2^{(1)}dx_2=bh^{(1)}e_{15}^{(1)}(\nu_{,3}+\psi)-bh^{(1)}\varepsilon_{11}^{(1)}\phi^1 \\ D_3^1=D_3^{[1]} & =b\int_{-h^{(1)}/2}^{h^{(1)}/2}x_2D_3^{(1)}dx_2=\frac{1}{12}b(h^{(1)})^3e_{33}^{(1)}\psi_{,3}-\frac{1}{12}b(h^{(1)})^3\varepsilon_{33}^{(1)}\phi_{,3}^1 \end{array} \tag{6}$$

Here, ϕ^1 represents the first-order distribution of electric potential, which can be expressed as the potential distribution per unit length. Similarly, n^1 represents the first-order change in electrons, which can be expressed as the distribution of the change in electron concentration per unit length. Thus the current relationship can be obtained by integrating over the cross-section:

$$\begin{array}{l} J_2^{n0}=J_2^{n[0]}=b\int_{-h^{(1)}/2}^{h^{(1)}/2}J_2^ndx_2=-bh^{(1)}qn_0\mu_{22}^n\phi^1+qbh^{(1)}D_{22}^nn^1 \\ J_3^{n1}=J_3^{n[1]}=b\int_{-h^{(1)}/2}^{h^{(1)}/2}x_2J_3^ndx_2=-\frac{1}{12}b(h^{(1)})^3qn_0\mu_{33}^n\phi_{,3}^1+\frac{1}{12}b(h^{(1)})^3qD_{33}^nn_{,3}^1 \\ J_2^{p0}=J_2^{p[0]}=b\int_{-h^{(1)}/2}^{h^{(1)}/2}J_2^pdx_2=-bh^{(1)}qp_0\mu_{22}^n\phi^1-qbh^{(1)}D_{22}^np^1 \\ J_3^{p1}=J_3^{p[1]}=b\int_{-h^{(1)}/2}^{h^{(1)}/2}x_2J_3^pdx_2=-\frac{1}{12}b(h^{(1)})^3qp_0\mu_{33}^n\phi_{,3}^1-\frac{1}{12}b(h^{(1)})^3qD_{33}^np_{,3}^1 \end{array} \tag{7}$$

Drawing on the fundamental principles of piezoelectricity, we present an exposition of the electromechanical coupling characteristics of PS structures, utilizing a Cartesian tensor system to formulate a set of three-dimensional differential equations. The resulting field equations incorporate the equations of motion, Gauss's theorem in electrostatics, and the continuity equations for the hole and electron charges are shown below [35–37]:

$$\begin{aligned} &T_{ji,j} = \rho \ddot{u}_i \\ &D_{i,i} = q(p - n + N_D^+ - N_A^-) \\ &J_{i,i}^p = -q\dot{p} \\ &J_{i,i}^n = q\dot{n} \end{aligned} \tag{8}$$

Assuming that the middle layer of the structure in Figure 2 is an n-type PS fiber, the field equation in static equilibrium can be written as:

$$\begin{aligned} &Q_{,3} = 0 \\ &M_{,3} - Q = 0 \\ &D_{3,3}^1 - D_2^0 = -\tfrac{1}{12} qb(h^{(1)})^3 n^1 \\ &J_{3,3}^{n1} - J_2^{n0} = 0 \end{aligned} \tag{9}$$

Substituting Equation (6) and (7) into Equation (9), the following four linear differential equations of second order concerning ν, ψ, and n^1 are obtained:

$$\begin{aligned} &(2bh^{(2)}c_{44}^{(2)} + bh^{(1)}c_{44}^{(1)})(\nu_{,33} + \psi_{,3}) + bh^{(1)}e_{15}^{(1)}\phi_{,3}^1 = 0 \\ &\tfrac{2}{3}[(\tfrac{h^{(1)}}{2} + h^{(2)})^3 - (\tfrac{h^{(1)}}{2})^3]bc_{33}^{(2)}\psi_{,33} + \tfrac{2}{3}(\tfrac{h^{(1)}}{2})^3 bc_{33}^{(1)}\psi_{,33} + \tfrac{2}{3}(\tfrac{h^{(1)}}{2})^3 be_{33}^{(1)}\phi_{,33}^1 \\ &-(2bh^{(2)}c_{44}^{(2)} + bh^{(1)}c_{44}^{(1)})(\nu_{,3} + \psi) - bh^{(1)}e_{15}^{(1)}\phi^1 = 0 \\ &\tfrac{1}{12}b(h^{(1)})^3 e_{33}^{(1)}\psi_{,33} - \tfrac{1}{12}b(h^{(1)})^3\varepsilon_{33}^{(1)}\phi_{,33}^1 - bh^{(1)}e_{15}^{(1)}(\nu_{,3} + \psi) + bh^{(1)}\varepsilon_{11}^{(1)}\phi^1 = -\tfrac{1}{12}qb(h^{(1)})^3 n^1 \\ &-\tfrac{1}{12}b(h^{(1)})^3 qn_0\mu_{33}^n\phi_{,33}^1 + \tfrac{1}{12}b(h^{(1)})^3 qD_{33}^n n_{,33}^1 + bh^{(1)}qn_0\mu_{22}^n\phi^1 - qbh^{(1)}D_{22}^n n^1 = 0 \end{aligned} \tag{10}$$

The solution of the above equation can be set in the following form:

$$\{\nu, \psi, \phi^1, n^1\} = \{N_1, N_2, N_3, N_4\}\exp(\lambda x_3) \tag{11}$$

Substituting the above equation into Equation (10) yields a homogeneous linear system of equations with unknown coefficients N_1 through N_4. To obtain non-trivial solutions, the determinant of the coefficient matrix is set to zero, resulting in an 8th-degree polynomial equation concerning λ. The eight roots of this equation are denoted as λ^m for $m = 1$ to 8, and the corresponding eigenvectors are represented as N_1^m-N_4^m. The ratios between these eigenvectors can be determined. Subsequently, the solution of Equation (10) is:

$$\begin{Bmatrix} \nu \\ \psi \\ \phi^1 \\ n^1 \end{Bmatrix} = \sum_{m=1}^{8} G^m \begin{Bmatrix} N_1^m \\ N_2^m \\ N_3^m \\ N_4^m \end{Bmatrix} \exp(\lambda^m x_3) \tag{12}$$

Here, G_m represents the unknown parameters. Equation (12) holds for both left and right sections of the multi-segmented layered structure model in Figure 2. However, the difference in equivalent stiffness results in different values of the coefficients in the two sections. Therefore, there are 16 parameters. They can be determined using the following boundary and continuity conditions:

$$\begin{array}{llll} \nu(0)=0, & \psi(0)=0, & D_3^1(0)=0, & J_3^{n1}(0)=0, \\ \nu(L_1^+)=\nu(L_1^-), & \psi(L_1^+)=\psi(L_1^-), & D_3^1(L_1^+)=D_3^1(L_1^-), & J_3^{n1}(L_1^+)=J_3^{n1}(L_1^-), \\ M(L_1^+)=M(L_1^-), & Q(L_1^+)=Q(L_1^-), & \phi^1(L_1^+)=\phi^1(L_1^-), & n^1(L_1^+)=n^1(L_1^-), \\ M(L_2)=0, & Q(L_2)=F, & D_3^1(L_2)=0, & J_3^{n1}(L_2)=0, \end{array} \tag{13}$$

This section deduced the one-dimensional coupled system of differential equations for the multi-segmented layered structure. By integrating the appropriate boundary conditions and solving for the coefficient matrix, the following quantities can be determined: deflection ν, shear deformation ψ, electric potential ϕ^1, electron concentration variation n^1.

3 Example analysis

Initially, we conducted a correctness validation. In the absence of an additional layer, our model simplifies to a piezoelectric semiconductor cantilever beam under bending. By employing parameters identical to those in Zhang's paper [38], we obtained identical results, as shown in Figure 3. Thus, the validity of our approach has been verified.

3.1 Effect of the elastic constant c_{33}

In the one-dimensional model established in Section 2, there are two elastic constants, c_{33} and c_{44}, related to bending deformation. We will separately consider the effects of these two parameters on the force-electric field distribution in the structure due to discontinuities. The structure has a length of $l = 600\ nm$ ($L_1 = 300\ nm$, $L_2 = 600\ nm$), a width of $b = 10\ nm$, a height of $h^{(1)} = 50\ nm$, and $h^{(2)} = 30\ nm$ with a ZnO n-type PS layer, whose material constants are listed in Table 1 [39], and an initial free electron concentration of $n_0 = 10^{21}\ m^{-3}$.

First, the effect of the discontinuity in the elastic constant c_{33} on the distribution of the electromechanical fields is investigated. It is assumed that $c_{44}^{(2l)} = c_{44}^{(2r)} = 3c_{44}^{(1)}$, which means that the elastic constant of the elastic layer $c_{44}^{(2)}$ is fixed at three times that of the piezoelectric layer $c_{44}^{(1)}$. The value of $c_{33}^{(2l)}$ is fixed at $3c_{33}^{(1)}$, and $c_{33}^{(2l)}$ varies from $1c_{33}^{(1)}$ to $5c_{33}^{(1)}$.

When an external force $F = 1\ nN$ is applied, Figure 4 shows the distribution of some electromechanical fields in the structure. When the material is uniformly distributed along the axial direction, the distribution of the fields is consistent with the distribution of the internal fields of a homogeneous ZnO fiber when it is bent, as reported in the literature [40]. The potential ϕ^1 and electron concentration n^1, change drastically only near the left end face, while

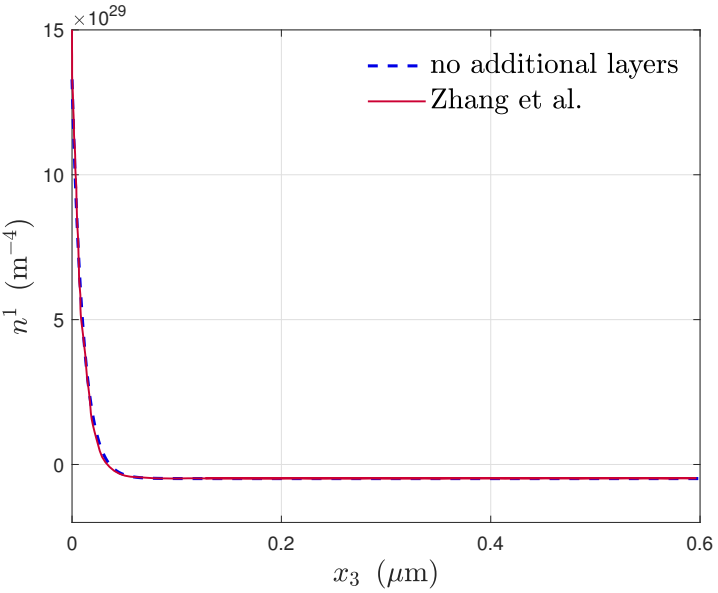

Figure 3: Comparison of the electron concentration variation n^1 distribution for a PS cantilever beam under bending without additional layers.

Table 1: Material constants of ZnO

Notation	Description	Value
$c_{33}^{(1)}$	Elastic constant	144.09 GPa
$c_{44}^{(1)}$	Elastic constant	42.43 GPa
$e_{33}^{(1)}$	Piezoelectric constant	1.68 C/m^2
$e_{15}^{(1)}$	Piezoelectric constant	-0.48 C/m^2
$\varepsilon_{33}^{(1)}$	Dielectric constant	11.19×10^{-11} F/m
$\varepsilon_{11}^{(1)}$	Dielectric constant	7.57×10^{-11} F/m

remaining constant in the rest of the structure. This is a typical electrical characteristic of a bent PS fiber.

When the value of $c_{33}^{(2r)}$ changes, there is a jump in the elastic constant of the fiber at the center. The overall potential and electron concentration of the fiber no longer remain unchanged. Instead, a potential barrier or well is generated at the interface between attached layers, and there is a potential difference between the two sides of the interface, indicating that the potential in the middle of the fiber can be controlled. The jump in elastic constant also leads to a separation between the deflection curve ν in Figure 4(a) and the angle of rotation ψ in Figure 4(b) at the interface. When $c_{33}^{(2r)}$ increases, the deformation of the structure becomes difficult, resulting in a decrease in the

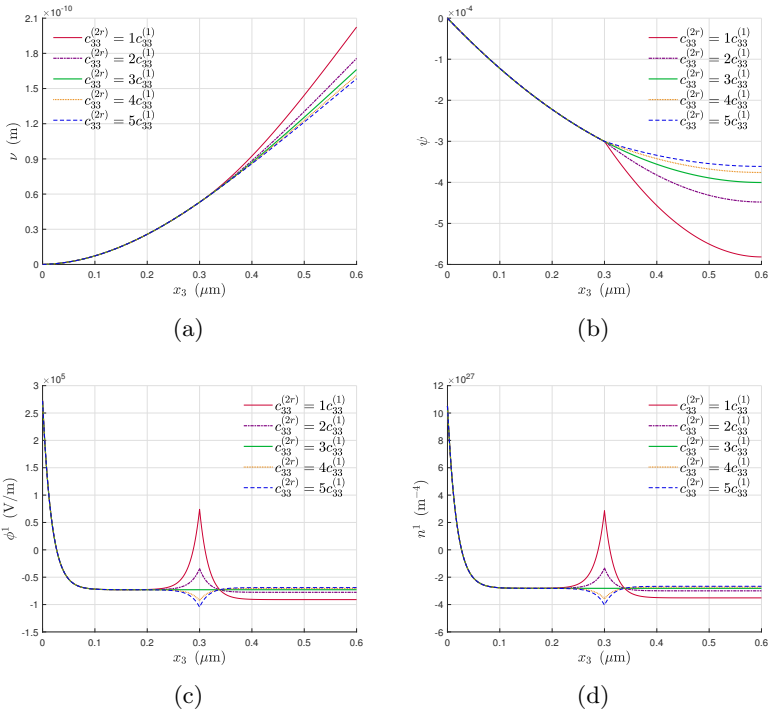

Figure 4: Effect of discontinuity in elastic constants $c_{33}^{(2r)}$ on electromechanical field distribution: (a) deflection ν; (b) shear deformation ψ; (c) electric potential ϕ^1; (d) electron concentration variation n^1.

deflection and rotation on the right side. At the same time, potential wells appear in both Figure 4(c) and Figure 4(d), and the greater the difference in the elastic constants between the two sides, the sharper the potential well. Conversely, when $c_{33}^{(2r)}$ decreases, the deformation of the structure becomes easier, resulting in an increase in the deflection and rotation on the right side. Potential barriers appear in both Figure 4(c) and Figure 4(d), and similarly, the greater the difference in the elastic constants between the two sides, the sharper the potential barrier. When the difference in elastic constants is the same, the amplitude of the potential barrier is higher compared to the potential well.

It is worth noting that the potential and electron concentration distributions in the region near the fixed end of the fiber overlap, and the change only occurs near the interface between attached layers. When $c_{33}^{(2r)}$ is greater than $c_{33}^{(2l)}$, a potential well is generated at the interface between attached layers, and the absolute value of the potential well increases as $c_{33}^{(2r)}/c_{33}^{(2l)}$ increases.

We can understand the influence of the elastic constants of the additional layers on the variation of the piezoelectric potential in the following way: The

presence of the heterogeneous elastic layers added to the homogeneous fiber introduces discontinuities in the overall axial stiffness of the structure. Under the influence of shear forces at the right end, strain also experiences interruptions at the points of stiffness transitions. Consequently, this further disrupts the continuity of polarization intensity, leading to the generation of polarization charges at the interfaces. Together with the volume charges arising from the polarization gradient, these interface polarization charges compel nearby free charge carriers to redistribute through electrostatic forces. As a result, local potential variations occur, giving rise to the formation of potential barriers and wells. This offers a design concept for nanoscale piezoelectric devices capable of harvesting local piezopotential energy.

3.2 Effect of the elastic constant c_{44}

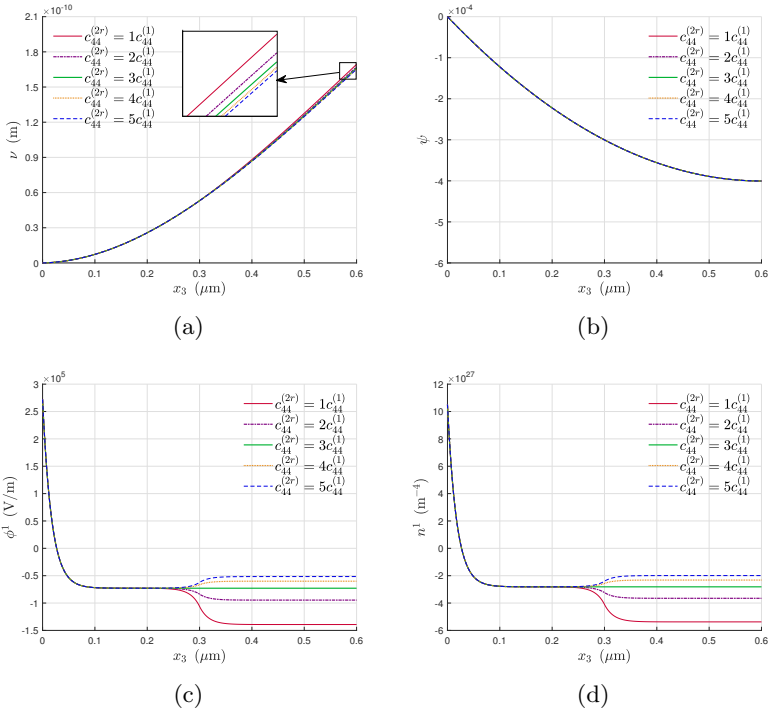

Figure 5: Effect of discontinuity in elastic constants $c_{44}^{(2r)}$ on electromechanical field distribution: (a) deflection ν; (b) shear deformation ψ; (c) electric potential ϕ^1; (d) electron concentration variation n^1.

This subsection investigates the effect of the discontinuity in the elastic constant c_{44} on the distribution of the electromechanical fields. It is assumed

that $c_{33}^{(2l)} = c_{33}^{(2r)} = 3c_{33}^{(1)}$, indicating that the elastic constant of the elastic layer $c_{33}^{(2)}$ remains constant along the axial direction and is three times that of the PS layer $c_{33}^{(1)}$. Only the value of $c_{44}^{(2r)}$ is varied, while the value of $c_{44}^{(2l)}$ fixed value is set at $3c_{44}^{(1)}$. When an external force $F = 1\ nN$ is applied, the distribution of the electromechanical fields in the structure is shown in Figure 5. In Figure 5(a) and 5(b), for different values of $c_{44}^{(2l)}$, the change in the deflection ν is very small, while the rotation angle ψ hardly changes and the curves overlap. In Figure 5(c) and 5(d), similar to changing c_{33}, the potential ϕ^1 and electron concentration variation n^1 on the left side remain almost unchanged, and the change only occurs near the interface between attached layers. The potential ϕ^1 and the change in electron concentration n^1 vary in the middle of the fiber. However, unlike in Figure 4(c) and 4(d), the distribution of ϕ^1 and n^1 does not show sharp steps or wells but forms a slowly varying platform barrier or well. That is, ϕ^1 and n^1 do not return to positions close to their original values after reaching their extremum, but remain stable.

It is noteworthy that when $c_{44}^{(2r)}$ is less than $c_{44}^{(2l)}$, the absolute value of the potential on the right platform area is higher than that on the left, and the larger the ratio of $c_{44}^{(2r)}/c_{44}^{(2l)}$, the greater the ratio of the absolute value of the potential, which has a guiding significance for piezoelectric devices that collect local potentials. This also indicates that using different structural configurations can produce various forms of local characteristics of the bent PS fiber. Of course, in actual devices, when materials with different elastic constants are used for the two sections of the attached layers in the structure, the jumps in c_{33} and c_{44} will occur simultaneously. Therefore, the form of potential variation should be a combination of sharp steps or wells and platform barriers or wells, and its specific form needs to be designed based on actual needs.

3.3 Two-dimensional field distribution

The distribution of the piezoelectric field in the bent fiber studied in this article is not one-dimensional, but varies in the two-dimensional x_3-x_2 plane. To illustrate the field variation more clearly, this subsection presents a plot of the distribution of the piezoelectric field in the fiber under flexural deformation.

Therefore, when considering the sharp potential wells and barriers that appear in the bent PS fiber as shown in Figure 4(c) and the platform potential wells and barriers that appear in Figure 5(c), we cannot isolate them and need to consider the influence of the two-dimensional distribution of the piezoelectric field on the potential energy.

To highlight the influence of different elastic constant discontinuities on the two-dimensional field distribution, we consider the following three situations:

I. $c_{33}^{(2l)} = c_{33}^{(2r)} = 3c_{33}^{(1)}$ and $c_{44}^{(2l)} = c_{44}^{(2r)} = 3c_{44}^{(1)}$, i.e., no jump in the material parameters;

II. $c_{33}^{(2l)} = 3c_{33}^{(2r)} = 3c_{33}^{(1)}$ and $c_{44}^{(2l)} = c_{44}^{(2r)} = 3c_{44}^{(1)}$, i.e., only a jump exists in $c_{33}^{(2)}$ and $c_{44}^{(2)}$ is constant;

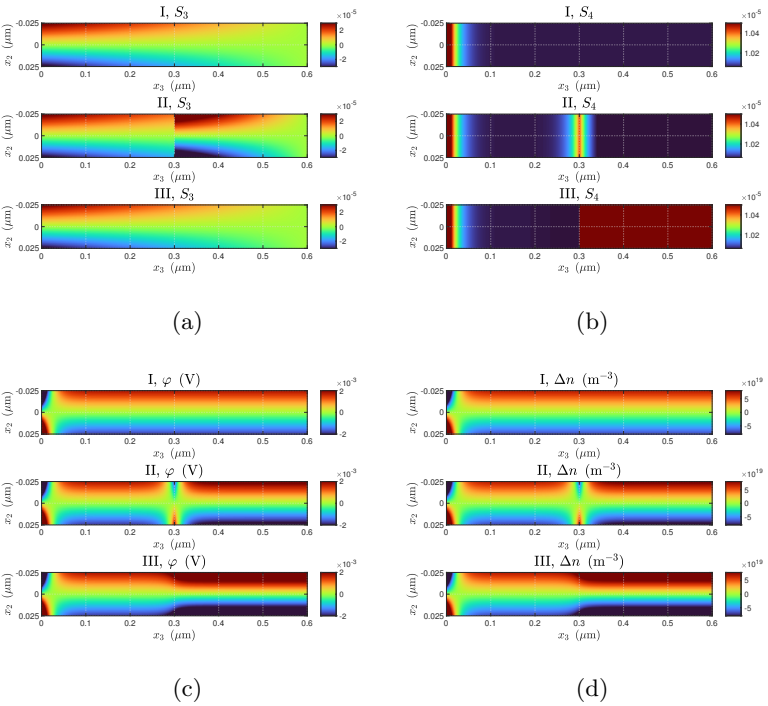

Figure 6: Two-dimensional field distribution in three cases: (a) normal strain S_3; (b) shear strain S_4; (c) electric potential ϕ; (d) electron concentration variation Δn. In each subfigure, I represents $c_{33}^{(2l)} = c_{33}^{(2r)} = 3c_{33}^{(1)}$ and $c_{44}^{(2l)} = c_{44}^{(2r)} = 3c_{44}^{(1)}$; II represents $c_{33}^{(2l)} = 3c_{33}^{(2r)} = 3c_{33}^{(1)}$ and $c_{44}^{(2l)} = c_{44}^{(2r)} = 3c_{44}^{(1)}$; III represents $c_{33}^{(2l)} = c_{33}^{(2r)} = 3c_{33}^{(1)}$ and $c_{44}^{(2l)} = 3c_{44}^{(2r)} = 3c_{44}^{(1)}$.

III. $c_{33}^{(2l)} = c_{33}^{(2r)} = 3c_{33}^{(1)}$ and $c_{44}^{(2l)} = 3c_{44}^{(2r)} = 3c_{44}^{(1)}$, i.e., only a jump exists in $c_{44}^{(2)}$ and $c_{33}^{(2)}$ is constant.

When $F = 1\ nN$, the comparison of some electromechanical field distributions in the fiber for these three cases is shown in Figure 6.

In Figure 6, the top, middle, and bottom layers of each image represent situations I, II, and III, respectively. As can be seen from the figure, due to the concentration of forces acting on the left end as a fixed support, the left side experiences a significant variation in the electromechanical field, which is not the focus of our research. The variation of the electric field at the interface in the middle of the fiber is the main focus of our study, and subsequent discussions will revolve around this. It is observed that the upper and lower segments of the piezoelectric semiconductor layer generate opposing and symmetrical electric fields. This phenomenon arises due to the bending deformation of the

fiber under shear forces at its end-faces, leading to the upper and lower portions of the fiber experiencing equal in magnitude yet opposite compressive and tensile forces.

First, we discuss the field distribution corresponding to situation I in the top layer of each image. In Figure 6(a), the normal strain S_3 has opposite signs on the upper and lower sides of the neutral plane where the strain is zero, which is because one side of the beam is stretched while the other side is compressed during the flexural deformation. The right end face of the structure only bears shear force in the x_2 direction, so the normal strain near it is close to zero. In Figure 6(b), the shear strain along the x_2 direction is unchanged because the one-dimensional assumption we adopted assumes that the cross-section of the fiber remains plane before and after deformation. In Figure 6(c), the sign of the electric potential φ is opposite on both sides of the neutral plane, and it hardly changes along the axial direction. This is consistent with the calculation results in reference [16] and is a typical feature of the electric potential distribution in a bent PS fiber. The distribution of the change in electron concentration Δn in Figure 6(d) is also the same. The field distributions for the discontinuous $c_{33}^{(2)}$ in case II are shown in the middle layer of each image in Figure 6.

It can be seen that the normal strain S_3 undergoes a discontinuous jump at the discontinuity of $c_{33}^{(2)}$, while the distribution of the shear strain S_4 becomes non-uniform but does not produce a discontinuous jump. The electric potential φ and the change in electron concentration Δn exhibit sharp wells and barriers on both sides of the neutral plane, which is consistent with the results in Figure 4(c) and 4(c). For the third situation shown in the bottom layer of Figure 6, the discontinuity in $c_{44}^{(2)}$ causes a jump in the shear strain, while the normal strain remains continuous. This is exactly the opposite of the situation when $c_{33}^{(2)}$ is discontinuous. At this time, the middle section of φ and Δn no longer exhibit sharp wells or barriers but a relatively slow-changing platform.

When the multi-segmented layered structure is bent, the axial polarization intensity inside the PS fiber can be obtained by $P_3^{(1)} = D_3^{(1)} - \varepsilon_0 E_3$. The distributions of $P_3^{(1)}$ corresponding to case II (only $c_{33}^{(2)}$ has a jump) and case III (only $c_{44}^{(2)}$ has a jump) in Figure 6 are shown in Figure 7. As shown in Figure 7, when $c_{33}^{(2)}$ jumps, the axial polarization intensity is discontinuous at the interface. Additionally, interface polarization charges are generated here, and nearby free electrons are redistributed under the action of electrostatic force. Therefore, sharp potential wells and barriers appear in the electric potential φ, which is reflected in the electric potential distribution graph in the middle layer of Figure Figure 6(c). It is also shown in Figure 7 that, when $c_{44}^{(2)}$ jumps, although there is a small peak in the axial polarization intensity at the interface, there is no discontinuity. Therefore, there are no sharp potential wells or barriers in the electric potential distribution graph in the lower layer of Figure 6(c). The platform-like change is caused by the body polarization charges and the polarization charges on the upper and lower surfaces of the fiber.

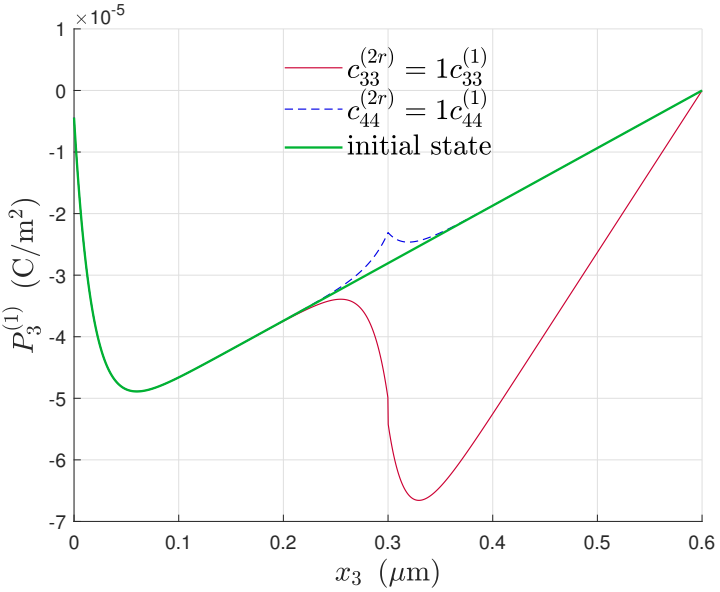

Figure 7: Distribution of axial polarization intensity $P_3^{(1)}$ during $c_{33}^{(2)}$ and $c_{44}^{(2)}$ jump;

3.4 Effect of the elastic layer thickness *h*

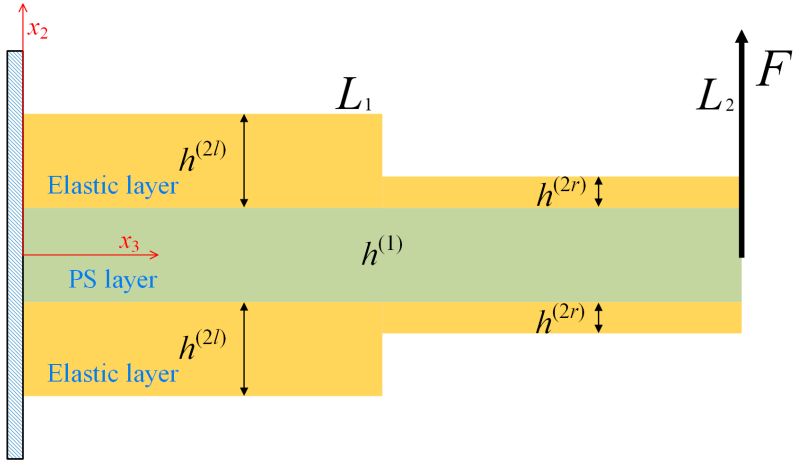

Figure 8: A schematic of the bent multi-segmented layered structure with varying elastic layer heights.

Previous studies were based on the assumption that the attached elastic layer has a constant thickness. In this subsection, the effect of the variation of the elastic layer thickness h on the distribution of the force-electric field is investigated. The PS model for the multi-segmented layered structure in this subsection is shown in Figure 8, where the elastic constants $c_{33}^{(2)}$ and $c_{44}^{(2)}$ of the elastic layer are fixed, and $c_{33}^{(2l)} = c_{33}^{(2r)} = 3c_{33}^{(1)}$ and $c_{44}^{(2l)} = c_{44}^{(2r)} = 3c_{44}^{(1)}$. The thickness $h^{(2)}$ of the elastic layer is divided into two parts, $h^{(2l)}$ and $h^{(2r)}$, on the left and right sides, respectively. The thickness of the left part $h^{(2l)}$ is fixed at 30 nm, while the thickness of the right part varies between 10 nm and 50 nm.

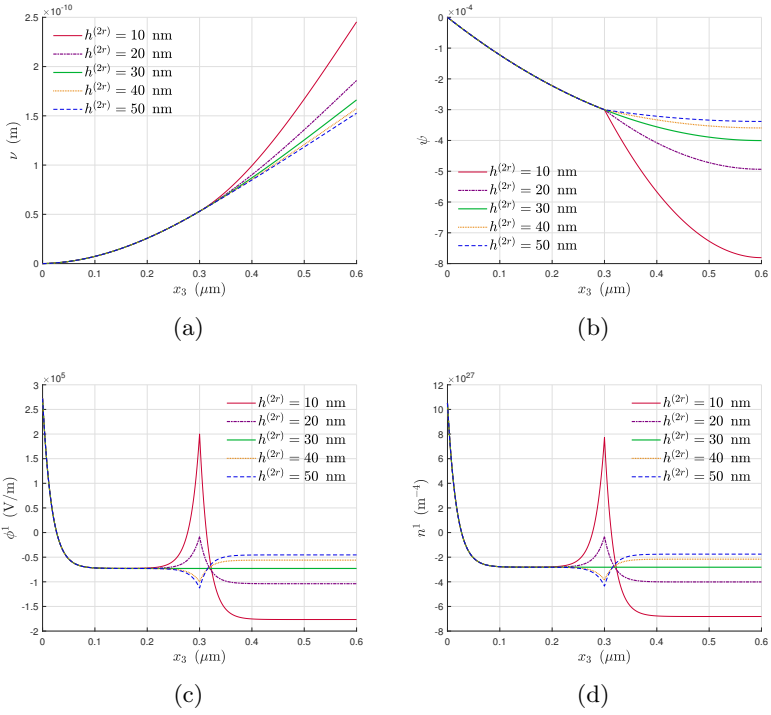

Figure 9: Effect of discontinuity in elastic constants $c_{33}^{(2r)}$ on electromechanical field distribution: (a) deflection ν; (b) shear deformation ψ; (c) electric potential ϕ^1; (d) electron concentration variation n^1.

The deflection ν in Figure 9(a) and the shear deformation ψ in Figure 9(b) both experience separation at the thickness transition. From a physical perspective, when the thickness $h^{(2)}$ of the attached elastic layer is small, the deformation of the structure is relatively easy, and the deflection ν and shear deformation ψ on the right side also increase accordingly. Figures 9(c) and 9(d) show the distribution of the potential ϕ^1 and the change in electron

concentration n^1 when the thickness changes. At the thickness transition, sharp potential wells or barriers appear in the potential ϕ^1 and the change in electron concentration n^1, and the sharpness depends on the thickness difference of the elastic layers on both sides. Furthermore, either a plateau-shaped potential barrier appears on the right side of the central potential well, or a plateau-shaped potential well appears on the right side of the central potential barrier.

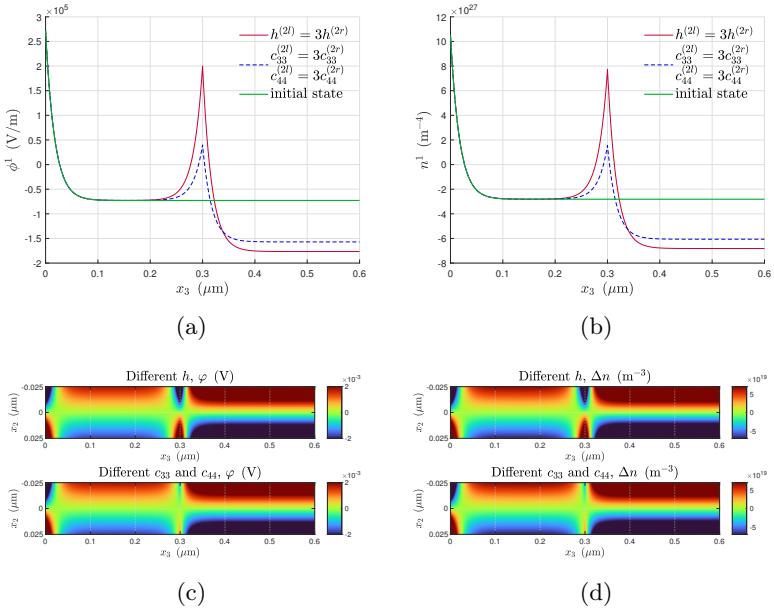

Figure 10: Comparison of the potential and carrier concentration changes between the case of a jump in height h and a simultaneous jump in material coefficients c_{33} and c_{44}. (a) electric potential ϕ^1; (b) electron concentration variation n^1. (c) two-dimensional electric potential φ; (d) two-dimensional electron concentration variation Δn.

It is noteworthy that this peculiar change in the electric field is similar to the combined effect of changing c_{33} in Subsection 3.1 and changing c_{44} in Subsection 3.2. To better compare the similarities and differences between changing the thickness h of the elastic layer and changing the elastic parameters c_{33} and c_{44} simultaneously, Figure 10 is selected to compare the case of $h^{(2l)} = 30\ nm$, $h^{(2r)} = 10\ nm$ and $c_{33}^{(2l)} = 3c_{33}^{(2r)} = 3c_{33}^{(1)}$, $c_{44}^{(2l)} = 3c_{44}^{(2r)} = 3c_{44}^{(1)}$.

Figures 10(a) and 10(b) compare the distribution of potential and change in electron concentration, where the solid green line represents the initial state with uniform elastic layer height and no elastic coefficient changes. It can be seen from the figures that the effect of changing the thickness and changing the elastic coefficients c_{33} and c_{44} simultaneously on the trend of electric field

distribution is similar, but there are slight differences in amplitude changes. Figures 10(c) and 10(d) show the two-dimensional field distribution of the electric field, where it can be seen more clearly that the potential wells and barriers caused by thickness discontinuities are sharper. From the surface potential distribution, the fiber surface shows a multi-segment distribution, such as a low potential well plateau area, a sharp potential barrier area, and a high potential well plateau area on the lower surface of the fiber.

From the perspective of superposition, Figures 9(a) and 9(b) can also be understood as the similar result of simultaneous discontinuities in c_{33} and c_{44}. Since the discontinuity in c_{44} results in a very small change in the deflection ν and shear deformation ψ, the results are similar to that of the discontinuity of c_{33}, but the amplitude variation caused by the discontinuity of thickness h is larger.

Through the research in this subsection, we found that changing the thickness of the elastic layer can produce effects similar to simultaneously adjusting c_{33} and c_{44}. In practical design, it is almost impossible to adjust the elastic coefficients c_{33} and c_{44} of materials by changing the materials alone. This provides new insights and ideas for the design of PS structures and also provides new methods for obtaining the target ratio of c_{33} and c_{44}. For example, we can simultaneously change the thickness and material of the elastic layer on the right side to obtain the desired ratio of c_{33} and c_{44}, thereby better controlling the local potential in the piezoelectric fiber.

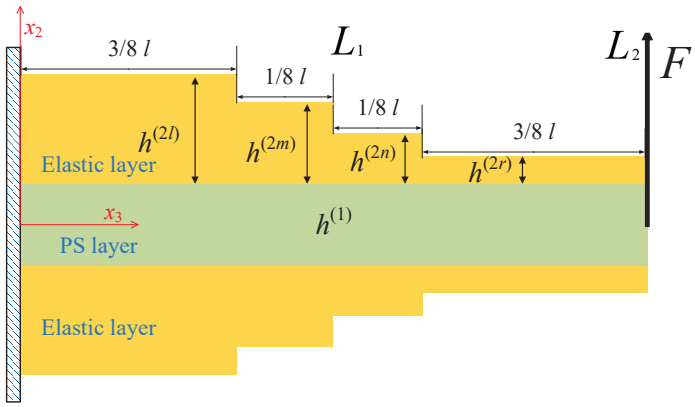

Figure 11: Schematic representation of the model for the four-segment multilayer structure.

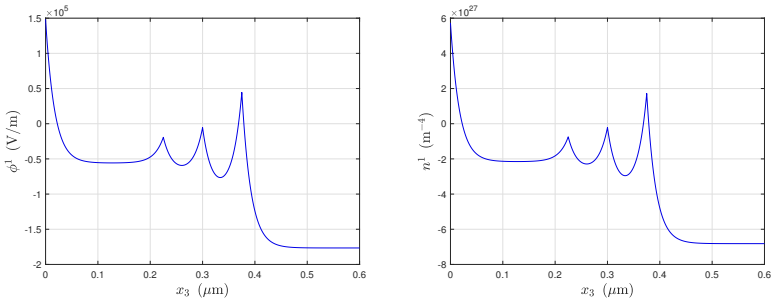

(a) (b)

Figure 12: Distribution of potential and carrier concentration changes for the four-segment multi-layer structure. (a) electric potential ϕ^1; (b) electron concentration variation n^1.

3.5 Structures with more segments

The multi-segmented layered fiber structure proposed in this paper can effectively regulate the local potential distribution for multi-layer structures consisting of more than three segments. Here, we take the example of a four-segment structure, with the structural model shown in Figure 11. The heights of the four segments, from left to right, are 40, 30, 20, and 10 nm. The segment boundaries are located at $3/8l$, $1/2l$, and $5/8l$. The potential and electron concentration distributions are presented in Figures Figure 12(a) and Figure 12(b), respectively. From the figures, it is evident that our design is capable of creating potential barriers or wells in local regions even for structures with more segments. This implies that our design exhibits enhanced generality.

4 Conclusion

The influence of a multi-segmented layered structure design on the local electromechanical coupling characteristics of a bent PS fiber was investigated in this paper. The one-dimensional coupled equation of the bent multi-segmented layered PS structure was solved. The electrical distributions of the PS fiber were analyzed by studying and discussing the numerical results. The distribution of potential and electron concentration for different elastic coefficient jumps in the attached layers was compared, and the similarities and differences were analyzed. The main conclusions of this paper are as follows:

(1) In the bent multi-segmented layered PS fiber, the discontinuity in material coefficients or attachment layer thickness breaks the uniformity of electrical characteristics in the intermediate region, allowing for active modulation in response to external forces.

(2) In bent multi-segmented layered PS fibers, the distribution of local potential wells and barriers varies along the axis and is symmetrical about the strain neutral axis.

(3) In bent multi-segmented layered PS fibers, the jumps in different material coefficients in the attached layer have different effects on the local potential changes. Specifically, the jump in c_{33} produces sharp local potential wells and barriers in the fiber, while the jump in c_{44} produces relatively flat platform-type potential wells and barriers. Meanwhile, the effect of the thickness variation of the attached layer is similar to the effect of the simultaneous variation of the material coefficients c_{33} and c_{44}. This suggests that local piezopotential regulation can be diversified through different materials and thicknesses combinations.

Acknowledgments

This work was supported by the National Natural Science Foundation of China (12061131013, 11972276, 12172171, and 12211530064), the State Key Laboratory of Mechanics and Control of Mechanical Structures at NUAA (No. MCMS-I-0522G01), the Fundamental Research Funds for the Central Universities (NS2022011 and NE2020002), National Natural Science Foundation of Jiangsu Province (BK20211176), Jiangsu High-Level Innovative and Entrepreneurial Talents Introduction Plan (Shuangchuang Doctor Program, JSSCBS20210166), and a project funded by the Priority Academic Program Development of Jiangsu Higher Education Institutions (PAPD). Prof. Iren E Kuznetsova thanks Russian Ministry of Science and Higher Education (government task FFWZ-2022-0002) for partial financial support.

Data Availability Statement

The data that support the findings of this study are available from the corresponding author upon reasonable request.

Declarations

Conflict of Interest

There are no conflicts of interest to disclose by the authors that are relevant to the content of this article.

References

[1] Wu, W., Wang, L., Li, Y., Zhang, F., Lin, L., Niu, S., Chenet, D., Zhang, X., Hao, Y., Heinz, T.F., Hone, J., Wang, Z.L.: Piezoelectricity of single-atomic-layer mos2 for energy conversion and piezotronics. Nature **514**(7253), 470–474 (2014). https://doi.org/10.1038/nature13792

[2] Hu, Y., Zhang, Y., Xu, C., Zhu, G., Wang, Z.L.: High-output nanogenerator by rational unipolar assembly of conical nanowires and its application for driving a small liquid crystal display. Nano Letters **10**(12), 5025–5031 (2010). https://doi.org/10.1021/nl103203u

[3] Wen, X., Wu, W., Ding, Y., Wang, Z.L.: Piezotronic effect in flexible thin-film based devices. Advanced Materials **25**(24), 3371–3379 (2013). https://doi.org/10.1002/adma.201300296

[4] Qin, Y., Wang, X., Wang, Z.L.: Microfibre-nanowire hybrid structure for energy scavenging. Nature **451**(7180), 809–813 (2008). https://doi.org/10.1038/nature06601

[5] Rajagopalan, P., Singh, V., Palani, I.A., Kim, S.J.: Superior response in zno nanogenerator via interfaced heterojunction for novel smart gas purging system. Extreme Mechanics Letters **26**, 18–25 (2019). https://doi.org/10.1016/j.eml.2018.11.004

[6] Wang, X., Zhou, J., Song, J., Liu, J., Xu, N., Wang, Z.L.: Piezoelectric field effect transistor and nanoforce sensor based on a single zno nanowire. Nano Letters **6**(12), 2768–2772 (2006). https://doi.org/10.1021/nl061802g

[7] Dahiya, R.S., Metta, G., Valle, M., Adami, A., Lorenzelli, L.: Piezoelectric oxide semiconductor field effect transistor touch sensing devices. Applied Physics Letters **95**(3) (2009). https://doi.org/10.1063/1.3184579

[8] Wu, J.M., Chen, K.H., Zhang, Y., Wang, Z.L.: A self-powered piezotronic strain sensor based on single znsno3 microbelts. RSC Advances **3**(47), 25184–25189 (2013). https://doi.org/10.1039/c3ra45027a

[9] Qi, J., Zhang, H., Lu, S., Li, X., Xu, M., Zhang, Y.: High performance indium-doped zno gas sensor. Journal of Nanomaterials **2015** (2015). https://doi.org/10.1155/2015/954747

[10] Wu, W., Wei, Y., Wang, Z.L.: Strain-gated piezotronic logic nanodevices. Advanced Materials **22**(42), 4711–4715 (2010). https://doi.org/10.1002/adma.201001925

[11] Momeni, K.: Enhanced mechanical properties of zno nanowire-reinforced nanocomposites: a size-scale effect. Acta mechanica **225**(9), 2549–2562 (2014). https://doi.org/10.1007/s00707-014-1086-4

[12] Yang, G.Y., Du, J.K., Wang, J., Yang, J.S.: Extension of a piezoelectric semiconductor fiber with consideration of electrical nonlinearity. Acta Mechanica **229**(11), 4663–4676 (2018). https://doi.org/10.1007/s00707-018-2216-1

[13] Pan, C.F., Zhai, J.Y., Wang, Z.L.: Piezotronics and piezo-phototronics of third generation semiconductor nanowires. Chemical Reviews **119**(15), 9303–9359 (2019). https://doi.org/10.1021/acs.chemrev.8b00599

[14] Wang, G.L., Liu, J.X., Liu, X.L., Feng, W.J., Yang, J.S.: Extensional vibration characteristics and screening of polarization charges in a zno piezoelectric semiconductor nanofiber. Journal of Applied Physics **124**(9), 10 (2018). https://doi.org/10.1063/1.5048571

[15] Jiao, F.Y., Wei, P.J., Zhou, X.L., Zhou, Y.H.: The dispersion and attenuation of the multi-physical fields coupled waves in a piezoelectric semiconductor. Ultrasonics **92**, 68–78 (2019). https://doi.org/10.1016/j.ultras.2018.09.009

[16] Fan, S.Q., Liang, Y.X., Xie, J.M., Hu, Y.T.: Exact solutions to the electromechanical quantities inside a statically-bent circular zno nanowire by taking into account both the piezoelectric property and the semiconducting performance: Part i-linearized analysis. Nano Energy **40**, 82–87 (2017). https://doi.org/10.1016/j.nanoen.2017.07.049

[17] Yang, W.L., Liu, J.X., Hu, Y.T.: Mechanical tuning methodology on the barrier configuration near a piezoelectric pn interface and the regulation mechanism on i-v characteristics of the junction. Nano Energy **81**, 12 (2021). https://doi.org/10.1016/j.nanoen.2020.105581

[18] Cheng, R.R., Zhang, C.L., Chen, W.Q., Yang, J.S.: Piezotronic effects in the extension of a composite fiber of piezoelectric dielectrics and non-piezoelectric semiconductors. Journal of Applied Physics **124**(6), 8 (2018). https://doi.org/10.1063/1.5044739

[19] Qu, Y.L., Jin, F., Yang, J.S.: Torsion of a flexoelectric semiconductor rod with a rectangular cross section. Archive of Applied Mechanics **91**(5), 2027–2038 (2021). https://doi.org/10.1007/s00419-020-01867-0

[20] Wang, X.D., Song, J.H., Liu, J., Wang, Z.L.: Direct-current nanogenerator driven by ultrasonic waves. Science **316**(5821), 102–105 (2007). https://doi.org/10.1126/science.1139366

[21] Lee, E., Park, J., Yim, M., Kim, Y., Yoon, G.: Characteristics of piezoelectric zno/aln-stacked flexible nanogenerators for energy harvesting applications. Applied Physics Letters **106**(2) (2015). https://doi.org/10.1063/1.4904270

[22] Johar, M.A., Hassan, M.A., Waseem, A., Ha, J.S., Lee, J.K., Ryu, S.W.: Stable and high piezoelectric output of gan nanowire-based lead-free piezoelectric nanogenerator by suppression of internal screening. Nanomaterials **8**(6) (2018). https://doi.org/10.3390/nano8060437

[23] Johar, M.A., Jeong, D.K., Hassan, M.A., Kang, J.H., Ha, J.S., Lee, J.K., Ryu, S.W.: Controlled carrier screening in p-n nio/gan piezoelectric generators by an al2o3 insertion layer. Journal of Physics D: Applied Physics

50(48) (2017). https://doi.org/10.1088/1361-6463/aa946a

[24] Lee, S., Hinchet, R., Lee, Y., Yang, Y., Lin, Z.H., Ardila, G., Montès, L., Mouis, M., Wang, Z.L.: Ultrathin nanogenerators as self-powered/active skin sensors for tracking eye ball motion. Advanced Functional Materials **24**(8), 1163–1168 (2014). https://doi.org/10.1002/adfm.201301971

[25] Le, A.T., Ahmadipour, M., Pung, S.Y.: A review on zno-based piezoelectric nanogenerators: Synthesis, characterization techniques, performance enhancement and applications. Journal of Alloys and Compounds **844** (2020). https://doi.org/10.1016/j.jallcom.2020.156172

[26] Dahiya, A.S., Morini, F., Boubenia, S., Nadaud, K., Alquier, D., Poulin-Vittrant, G.: Organic/inorganic hybrid stretchable piezoelectric nanogenerators for self-powered wearable electronics. Advanced Materials Technologies **3**(2) (2018). https://doi.org/10.1002/admt.201700249

[27] Hinchet, R., Lee, S., Ardila, G., Montès, L., Mouis, M., Wang, Z.L.: Performance optimization of vertical nanowire-based piezoelectric nanogenerators. Advanced Functional Materials **24**(7), 971–977 (2014). https://doi.org/10.1002/adfm.201302157

[28] Kong, D., Cheng, R., Zhang, C., Zhang, C.: Dynamic manipulation of piezotronic behaviors of composite multiferroic semiconductors through time-dependent magnetic field. Journal of Applied Physics **128**(6) (2020). https://doi.org/10.1063/5.0015957

[29] Dietz, D.R., Busse, L.J., Fife, M.J.: Acoustoelectric detection of ultrasound power with composite piezoelectric and semiconductor devices. IEEE Transactions on Ultrasonics, Ferroelectrics, and Frequency Control **35**(2), 146–151 (1988). https://doi.org/10.1109/58.4164

[30] Sharma, J.N., Sharma, K.K., Kumar, A.: Surface waves in a piezoelectric-semiconductor composite structure. International Journal of Solids and Structures **47**(6), 816–826 (2010). https://doi.org/10.1016/j.ijsolstr.2009.11.016

[31] Jiao, F., Wei, P., Zhou, Y., Zhou, X.: Wave propagation through a piezoelectric semiconductor slab sandwiched by two piezoelectric half-spaces. European Journal of Mechanics, A/Solids **75**, 70–81 (2019). https://doi.org/10.1016/j.euromechsol.2019.01.007

[32] Tiersten, H.F., Stevens, D.S.: An analysis of thickness-extensional trapped energy resonant device structures with rectangular electrodes in the piezoelectric thin film on silicon configuration. Journal of Applied Physics **54**(10), 5893–5910 (1983). https://doi.org/10.1063/1.331763

[33] Luo, Y., Zhang, C., Chen, W., Yang, J.: Piezotronic effect of a thin film with elastic and piezoelectric semiconductor layers under a static flexural loading. Journal of Applied Mechanics, Transactions ASME **86**(5) (2019). https://doi.org/10.1115/1.4042573

[34] He, J., Du, J., Yang, J.: Stress effects on electric currents in antiplane problems of piezoelectric semiconductors over a rectangular domain. Acta mechanica **233**(3), 1173–1185 (2022). https://doi.org/10.1007/s00707-022-03148-z

[35] Pierret, R.F., Neudeck, G.W.: Advanced Semiconductor Fundamentals vol. 6. Addison-Wesley Reading, MA, Boston (1987)

[36] Hutson, A.R., White, D.L.: Elastic wave propagation in piezoelectric semiconductors. Journal of Applied Physics **33**(1), 40–47 (1962). https://doi.org/10.1063/1.1728525

[37] Auld, B.A.: Application of microwave concepts to the theory of acoustic fields and waves in solids. IEEE Transactions on Microwave Theory and Techniques **17**(11), 800–811 (1969). https://doi.org/10.1109/TMTT.1969.1127070

[38] Zhang, C., Wang, X., Chen, W., Yang, J.: Bending of a cantilever piezoelectric semiconductor fiber under an end force. Advanced Structured Materials **90**, 261–278 (2018). https://doi.org/10.1007/978-3-319-77504-3_13

[39] Zhang, C.L., Wang, X.Y., Chen, W.Q., Yang, J.S.: An analysis of the extension of a zno piezoelectric semiconductor nanofiber under an axial force. Smart Materials and Structures **26**(2), 8 (2017). https://doi.org/10.1088/1361-665X/aa542e

[40] Zhang, C., Wang, X., Chen, W., Yang, J.: Bending of a cantilever piezoelectric semiconductor fiber under an end force. Advanced Structured Materials **90**, 261–278 (2018). https://doi.org/10.1007/978-3-319-77504-3_13